Nanotechnology Perceptions
ISSN 1660-6795
www.nano-ntp.com

A Comprehensive Study on the Correlation Between Structural, Magnetic and Morphological Behaviors of Ce3+ Substituted Cufe2o4 Nanoparticles

Akshay B. Ghumare[1], Maheshkumar L. Mane[1], Amarsinha B. Gorepatil[1], Sandip B. Deshmukh[2], Sagar E. Shirsath[3], R. H. Kadam[4], K. S. Lohar[4]

[1]Shikshan Maharshi Guruvarya R. G. Shinde Mahavidyalaya, Paranda Dist. Osmanabad (MS) INDIA
[2]Ramkrishana Paramhansa Mahavidyalaya Dharashiv (MS) INDIA
[3]Vivekanand College, Ch.Sambhajinagar (MS) INDIA
[4]Shrikrishana Mahavidyalaya Gunjoti Dist. Osmanabad (MS) INDIA

This study explores the influence of cerium (Ce3+) substitution on the structural, morphological, and magnetic properties of CuFe2O4 nanoparticles. Nano-crystalline Ce-doped copper ferrites, represented by the formula CuCexFe2-xO4 (where x ranges from 0.0 to 1.0 in increments of 0.2), were synthesized via the Sol-gel auto-combustion method. Comprehensive characterization of the samples was conducted using X-ray diffraction (XRD), Fourier-transform infrared spectroscopy (FTIR), field emission scanning electron microscopy, transmission electron microscopy, energy-dispersive X-ray spectroscopy (EDS), and X-ray photoelectron spectroscopy (XPS). XRD analysis revealed a single tetragonal ferrite phase for undoped CuFe2O4, which transitioned to mixed phases with increasing Ce3+ concentrations. FTIR spectra identified two prominent absorption bands between 400 and 600 cm-1, indicative of the ferrite structure. Variations in selected area electron diffraction (SAED) patterns were noted as a function of Ce3+ content. EDS and XPS analyses confirmed the stoichiometry and oxidation states of the elements, respectively. Notably, the magnetization measurements revealed a decrease in magnetization, attributed to the formation of a CeO2 secondary phase and the substitution of Fe3+ ions at the octahedral B-site with Ce ions. This research provides valuable insights into the modulation of ferrite nanoparticles' properties through cerium doping, with potential

implications for their application in various technological fields.
Keywords: Sol-gel, Magnetic materials, Secondary Phase, Nanoparticles, XPS.

1. Introduction

Spinel ferrite nanoparticles exhibit broad applicability in a variety of domains, including optoelectronics, sensing, and catalysis [(Bhalla et al., 2021)]. Additionally, spinel ferrite-based thin films exhibit potential applications in fields such as energy storage and random access memory [(Sagu et al., 2017)]. The significance of magnetic spinel ferrite nanoparticles in modern day technologies is demonstrated by their use in industrial electronic devices, water treatment, and biomedical applications [(Tahir Farid et al., 2018),(Kefeni et al., 2017),(Amiri et al., 2019)].

Jahn-Teller distortion makes ferromagnetic material-based copper ferrite nanoparticles an attractive candidate for further study [(Abdellatif et al., 2017),(Latiff et al., 2019)]. Due to their unique properties, these nanoparticles have attracted a lot of attention in the research community during the past two decades. Such features result from the combined effects of a small fraction of atoms in each crystalline core and a large fraction of atoms on the surface of the nanoparticles [(Rahimi-Nasrabadi et al., 2016)]. This peculiar combination has stimulated researchers to explore deeply into the characteristics and possible uses of copper ferrite nanoparticles.

In particular modifying the crystal chemistry of nanocrystalline magnetic materials has drawn a lot of attention. Several researchers reported the doping of different rare earth cations in spinel structure [(Meng et al., 2009),(Panda et al., 2003),(Bhowmik & Ranganathan, 2001),(Mahmoud & Sattar, 2004)].This interest has grown in recent years, notably in the context of rare earth (RE^{3+}) ion substitution inside copper ferrite nanoparticles. This evolving area of research has great potential for a number of cutting-edge technologies, which makes it an area of interest for academic research and innovation [(Panneer Muthuselvam & Bhowmik, 2010),(Bhosale et al., 1996),(Gadkari et al., 2009),(Kupferling et al., 2005),(Gadkari et al., 2010)]. Syntheses of ferrite nanoparticles are of great interest in the study and tailoring of specific magnetic properties. The magnetic behavior of nanocrystalline spinel ferrite is sensitive to the types of cation and their distribution amongst the two interstitial sites (A- and B- sites) of spinel lattice [(Borah & Ravi, 2021),(Andersen et al., 2018)]. Based on the ionic radius the RE^{3+} ions can be categorized into two types' viz. materials with radius closer to Fe and radius greater than Fe [(Rahimi-Nasrabadi et al., 2016)].

Due to variations in ionic radii, deformation in the spinel structure was observed. The substitution of Ce^{3+} at B- sites (octahedral) is bound to change the super exchange interaction and tune the magnetic properties of $CuFe_2O_4$[(Akhtar et al., 2021)]. The potential field of the surrounding ions barely affects the 4f orbital of the rare earth cerium (III) ion, as it's shielded by the $5S^2$ and $5P^6$ orbitals. Spinel ferrites can be doped with rare earth ions to enhance their electric and magnetic properties, also the occurrence of 4f-3d couplings determines the magneto crystalline anisotropy in ferrites [(Yang et al., 2007),(Shinde et al., 2012)].

In the present investigation we reported the sol-gel auto-combustion synthesis, structural, morphological and magnetic properties of Ce^{3+} substituted $CuFe_2O_4$: $CuCe_xFe_{2-x}O_4$ (x = 0.0 to

1.0 with steps of 0.2).

2. Experimental technique

Analytical grade metal cations of copper, cerium and ferric nitrate without further purification were used as starting material. The stoichiometric proportion of $Cu(NO_3)_2{\bullet}3H_2O$, $Fe(NO_3)_3{\bullet}9H_2O$ and $Ce(NO_3)_3{\bullet}6H_2O$ is used as starting material, citric acid ($C_6H_8O_7$) was used as fuel for combustion process. Ammonia (NH_3) was added to maintain the pH of the solution.

Cerium (III) substituted copper ferrite nanostructure with chemical formula $CuCe_xFe_{2-x}O_4$ (x = 0.0 to 1.0 with steps of 0.2) was fabricated by sol-gel auto-combustion method. Required weighed amount of starting reagents was taken to achieve the metal nitrate (M^{2+}/M^{3+}) molar ratio as 1:2. The metal nitrate to citric acid ratio was taken as 1:3 indicating fuel rich solutions. The mixture in their respective stoichiometric of metal nitrates and fuel was dissolved in deionized water. The ammonia solution slowly added to maintain the pH of the solution at 8. The viscous gel was obtained by continuous stirring and heating of the solution. Further after formation of viscous gel solution was ignited to form the lose powder by combustion.

The thermal behavior of ferrite nano particles was evaluated via thermogravimetric analysis (TGA) using a Perkin Elmer TG/DTA Diamond model. Using Cu-Kα radiation (λ = 1.5406 Å) on a PHILIPS diffractometer with θ-2θ geometry, X-ray powder diffraction (XRD) investigation showed the development of crystalline phases at room temperature. Scherrer's formula was used to calculate the average crystallite size from the X-ray diffraction data. Furthermore, Fourier transform infrared spectroscopy was performed at wave numbers between 400 and 4000 cm^{-1} in a KBr medium. Field emission scanning electron microscopy using model JSM-7600F revealed the surface morphology and chemical composition (EDS) of samples. The chemical state and elemental composition of elements was confirmed by X-ray photoelectron spectroscopy (XPS) using model AXIS supra. The pulse field hysteresis loop technique was used to perform the magnetic measurements at room temperature.

3. Results and discussion

3.1 Thermal Analysis

Thermo-chemical behavior of as-prepared cerium copper ferrite nanoparticles with chemical composition $CuCeFeO_4$ in the temperature range of ambient to 825 °C with heating rate of 5 °C/min were examined by TG/DTA and presented in Fig.1.

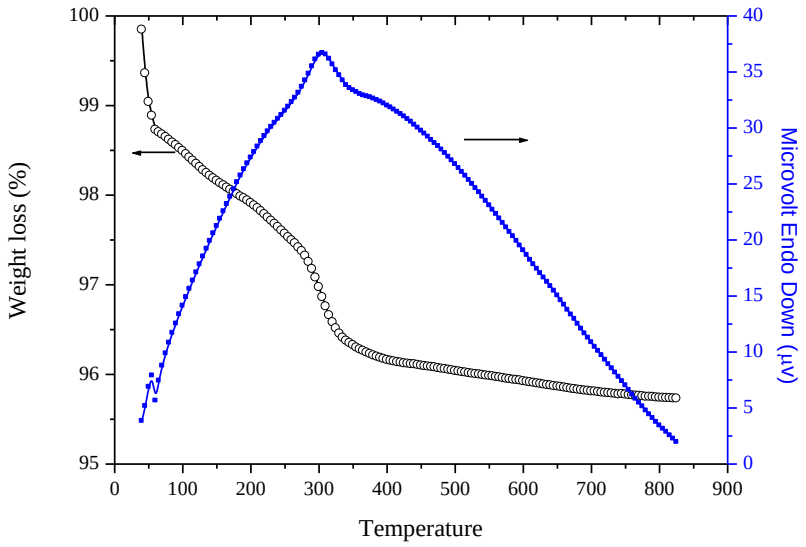

Figure 1: TG/DTA for as-prepared $CuCeFeO_4$

In the heat treatment of ferrite various processes like dehydration and decomposition of residual nitrate takes place. TGA curve represents different regions of weight loss, which are further confirmed by the occurrence of peaks on the DTA curve. In present case there are two endothermic peaks are observed. The first one is around 50-100^{o}c and second one is around 200-400^{o}c. The first peak is due to dehydration of absorbing water in sample and second one is due to decomposition of organic compounds and nitrates. The weight loss is found to be 4.153% at 303.71^{o}c which is due to dehydroxylation of ferrite materials. In DTA only one endothermic peak is observed at around 200-400 °C which is due to evaporation of water and decomposition of organic compounds and nitrates. No additional weight loss was observed at temperatures above the decomposition temperature (500°C), which reveals the proper formation of cerium doped copper ferrite nanoparticles.

3.2 X-ray Powder Diffraction

Crystalline phase formation confirmed by X-ray powder diffraction (XRD) pattern on PHILIPS diffractometer with θ-2θ geometry using Cu-K_α radiations (λ = 1.5406 Å) at room temperature, are shown in Figure 2.

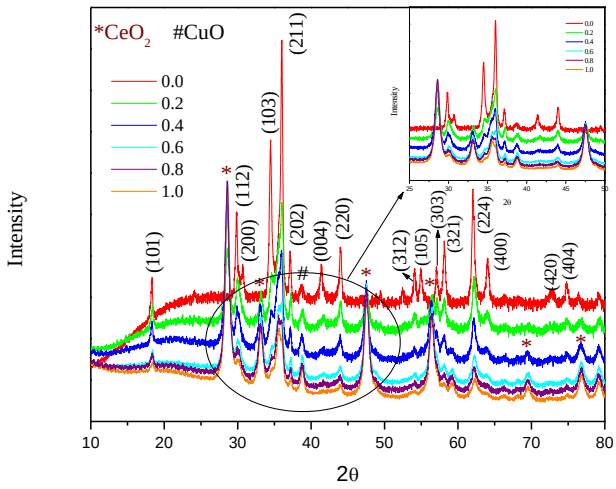

Figure 2: X-ray Diffraction Pattern for $CuCe_xFe_{2-x}O_4$ (x = 0.0, 0.2, 0.4, 0.6, 0.8 and 1.0)

A single tetragonal ferrite phase (For x = 0.0) appeared for copper ferrite nanoparticles, with no intermediate phase evident. Well-defined and broader diffraction peaks, all corresponding to characteristic crystallographic planes like (101), (112), (200), (103), (211), (202), (004) (220) (312), (105), (303), (321), (224), (400), (420) and (404) of the spinel structure was observed. All the diffraction peaks are well assigned to tetragonal structure of copper ferrite (JCPDS PDF# 34-0425). The diffraction peak broadening exhibits the nanocrystalline nature of the materials.

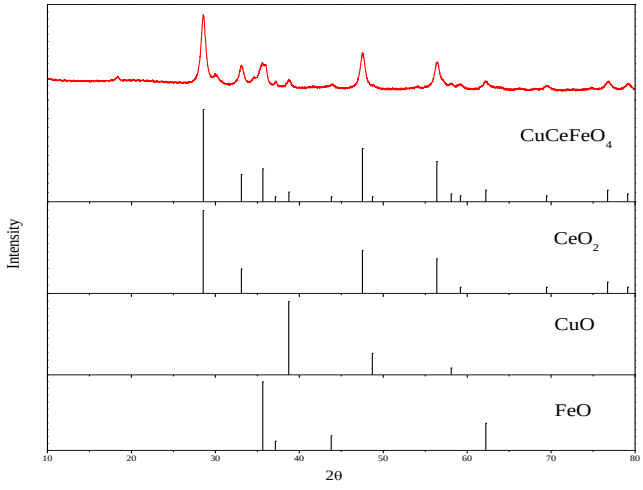

Figure 3: X-ray Diffraction Pattern indicating different Phases of $CuCeFeO_4$

During the early stage of cerium ion substitution in copper ferrite (x = 0.2 to 1.0 with steps of 0.2), a partial conversion to mixed phase from tetragonal phase occurred because Ce^{3+} ions with a larger radius (0.101 nm) replaces Fe^{3+} ions with a smaller radius (0.064 nm) in the octahedral site, which could create an internal stress to make the lattice distorted. Inset of Fig.2 indicates the formation of mixed phases due to Ce^{3+} ion substitution. XRD merely reveals a decrease of the intensity and an associated broadening of the Bragg peaks of the copper ferrite, which indicates formation of the disordered state. With increasing Ce^{3+} ion concentration, qualitative changes are observed in diffraction patterns of the samples and which may be due to the presence of a new phase, i.e., CeO_2. It is seen that, new sharp peaks (denoted by * in Fig.2) (111), (200), (220), and (311) observed, which corresponds to CeO_2 phase. The intensity of these peaks increased continuously with Ce^{3+} concentration, whereas the relative peak intensity corresponding to the planes (112), (103), (211), (202), (004), (220), (321) and (224) decreased. Similar results were reported by Subbiah Karthick et al. [(Subbiah et al., 2017)] for Ce doped nickel ferrite. For Ce^{3+} concentration with x = 1.0, X-ray diffraction data (Figure. 3) suggests the coexistence of three crystal phases in the sample, one of which closely corresponds to CeO_2 (JCPDS PDF# 34-0394), the second phase could be due to the formation of FeO (JCPDS PDF# 75-1550) and third phase corresponds to CuO (JCPDS PDF# 48-1548). This possibility of formation of three different phases was confirmed by XPS data analysis.

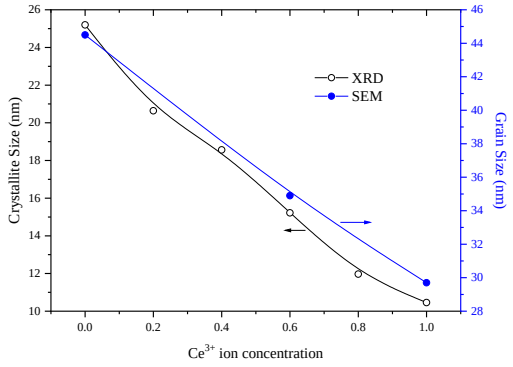

Figure4: Variation of crystallite size with Ce^{3+} ion concentration for $CuCe_xFe_{2-x}O_4$ (x = 0.0, 0.2, 0.4, 0.6, 0.8 and 1.0)

According to the Scherrer formula [(Cullity, 1978)], an average crystallite size of about 15 nm is derived from the full width at half maximum of the most intense peaks. Figure 4. shows the variation of crystallite size and observed that the crystallite size decreases with Ce^{3+} concentration.

3.3 Fourier Transform Infrared Spectroscopy

Fourier transform infrared (FTIR) spectra of ferrite system $CuCe_xFe_{2-x}O_4$ (x = 0.0, 0.2, 0.4, 0.6, 0.8 and 1.0) are shown in Fig.5. FTIR was recorded at room temperature in a KBr medium at wave numbers ranging from 400 to 4000 cm^{-1} exhibit two major absorption bands in the range 400 and 600 cm^{-1}.

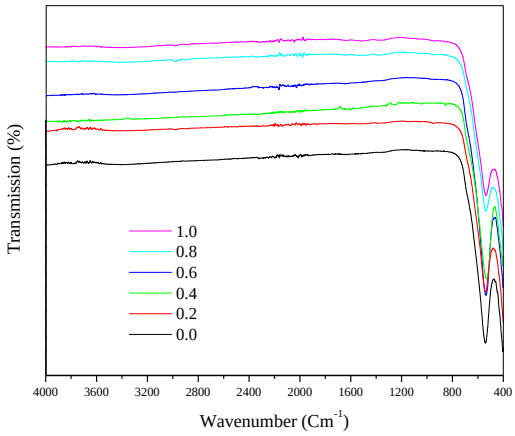

Figure 5: Fourier Transform Infrared spectra for $CuCe_xFe_{2-x}O_4$ (x = 0.0, 0.2, 0.4, 0.6, 0.8 and 1.0)

According to Waldron [(Jandl & Deslandes, 1981)] the vibration of unit cell of the spinel can be constructed in the tetrahedral (A) sites and octahedral (B) site. So, the absorption band (υ_1) is caused by scratching vibrations of the tetrahedral metal–oxygen bond and absorption band (υ_2) is caused by metal–oxygen vibrations in octahedral sites. From Fig.5 it is evident that the change in band position is exempted because of the difference in the Fe^{3+}–O^{2-} distances for the tetrahedral and octahedral complexes. Due to doping of Ce^{3+} ions, small shift in absorption band υ_2 was observed which indicates that the occupancy of Ce^{3+} on octahedral B site.

3.4 Morphological analysis

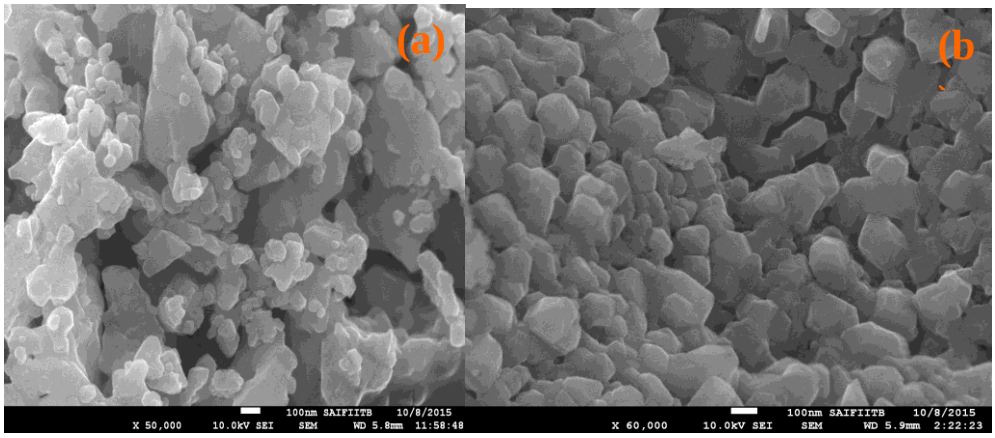

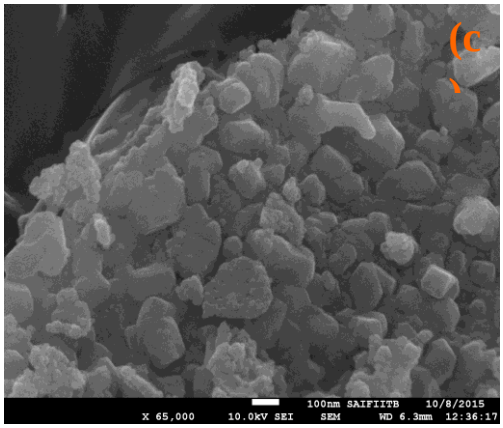

Figure 6: Field Emission Scanning Electron Microscopy (FESEM) Images for $CuCe_xFe_{2-x}O_4$ (a) x = 0.0, (b) x = 0.6 and (c) x = 1.0

The particle size and morphology of typical samples with x = 0.0, 0.6 and 1.0 is shown in Fig.6 and 7. SEM micrographs reveal that the particles of all samples have a similar morphology but different sizes (Figure 6). The particle size calculated from SEM images was found to be in close agreement with that obtained from XRD and variation with Ce^{3+} ion concentration is shown in Fig.4.

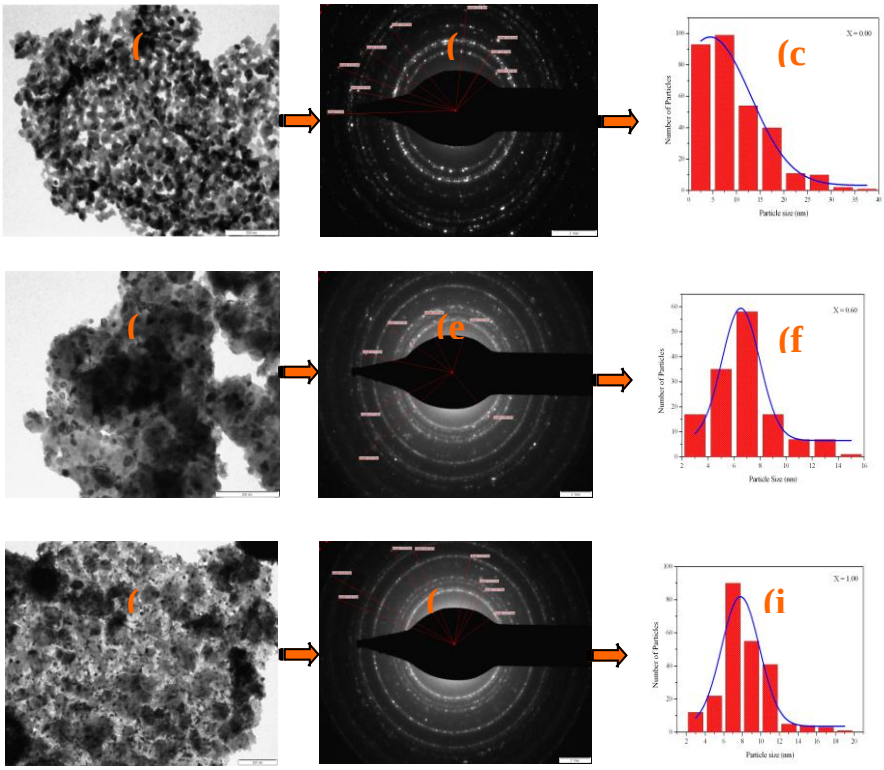

Figure 7: Transmission Electron Microscopy Images for $CuCe_xFe_{2-x}O_4$ (a) x = 0.0, (d) x =

0.6 and (g) x = 1.0

The morphology of typical samples of $CuCe_xFe_{2-x}O_4$ with x = 0.0, 0.6 and 1.0 was further investigated by transmission electron microscopy technique (TEM). The ring-like pattern in the selected area electron diffraction (SAED) (Fig.7 b) indicates that the $CuFe_2O_4$ nanoparticles and the most distinct concentric diffraction rings, which is consistent with the XRD results shown in Fig.2. As the Ce^{3+} concentration increases the changes in SAED diffraction rings was observed evaluating the mixed structure of ferrite samples.

The particle size of these samples was estimated by measuring the diameter of the particles from Gaussian fitting of Histograms. Fig.7 (c, f, i) represents the particle size distribution Gaussian fitting of Histograms, and average particle size is determined. The average particle size (10 nm) determined from Gaussian fitting is in close agreement with the particle size calculated from XRD and SEM analysis.

3.5 Energy Dispersive X-ray Spectroscopy (EDS)

The compositional stoichiometry of the $CuCe_xFe_{2-x}O_4$ (for x= 0.0 and 1.0) was investigated using EDS image analysis on various regions of the prepared samples, is shown in Fig.8. Composition determined by EDS is compared to the relative amount of metal cations ions used to make the particles of $CuCe_xFe_{2-x}O_4$. The percentage of iron is always found to be quite constant. Hence, the composition of Cu, Ce, Fe and O elements is similar to the composition of the mixture used for the synthesis.

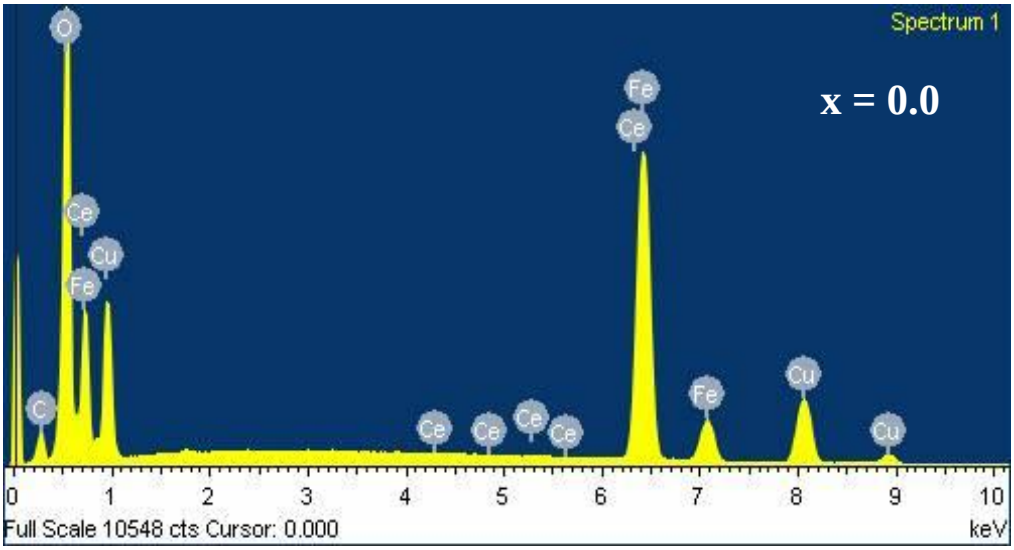

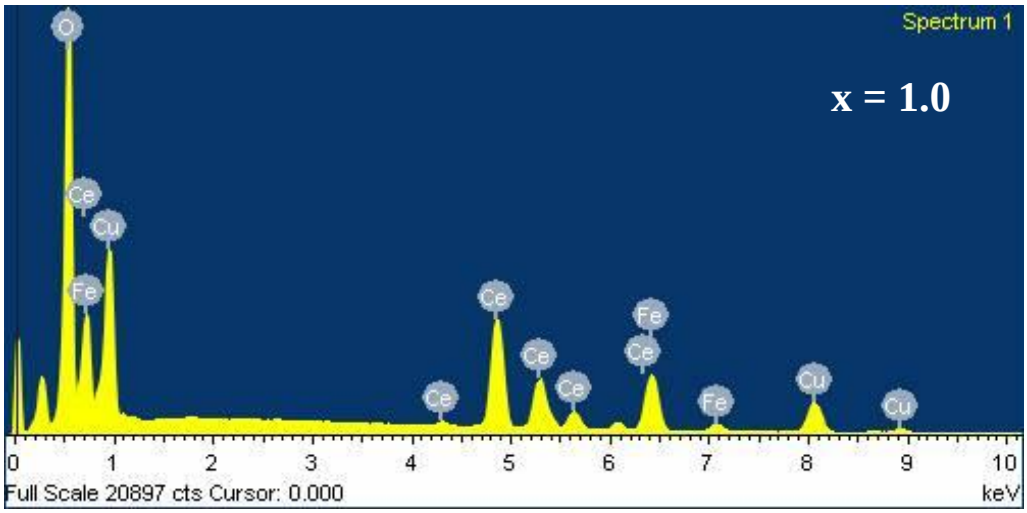

Figure 8: EDS Images for $CuCe_xFe_{2-x}O_4$ (For x = 0.0 and 1.0)

3.6 X-ray Photoelectron Spectroscopy (XPS)

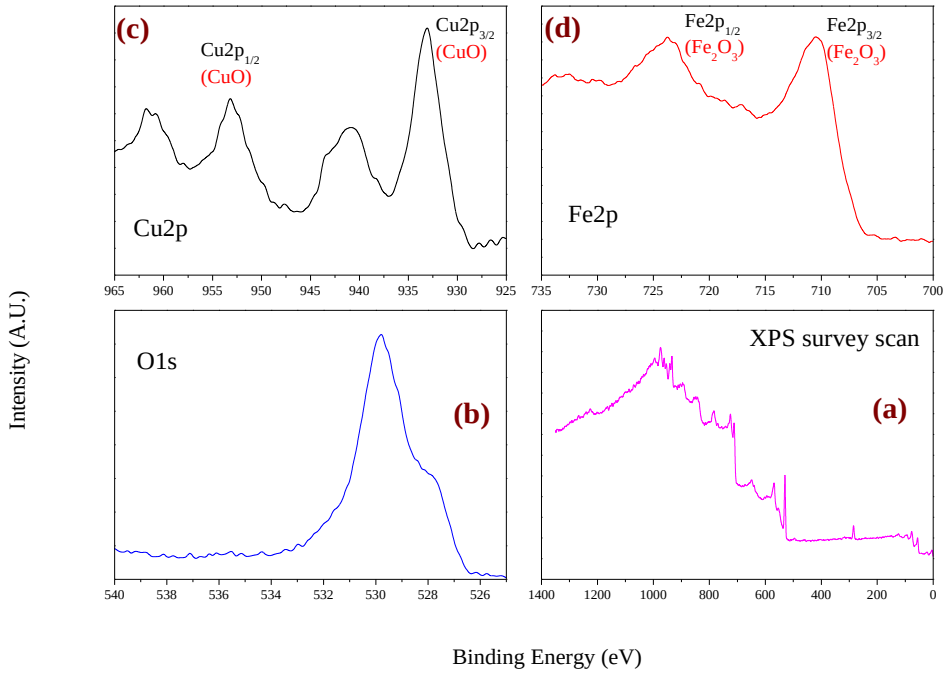

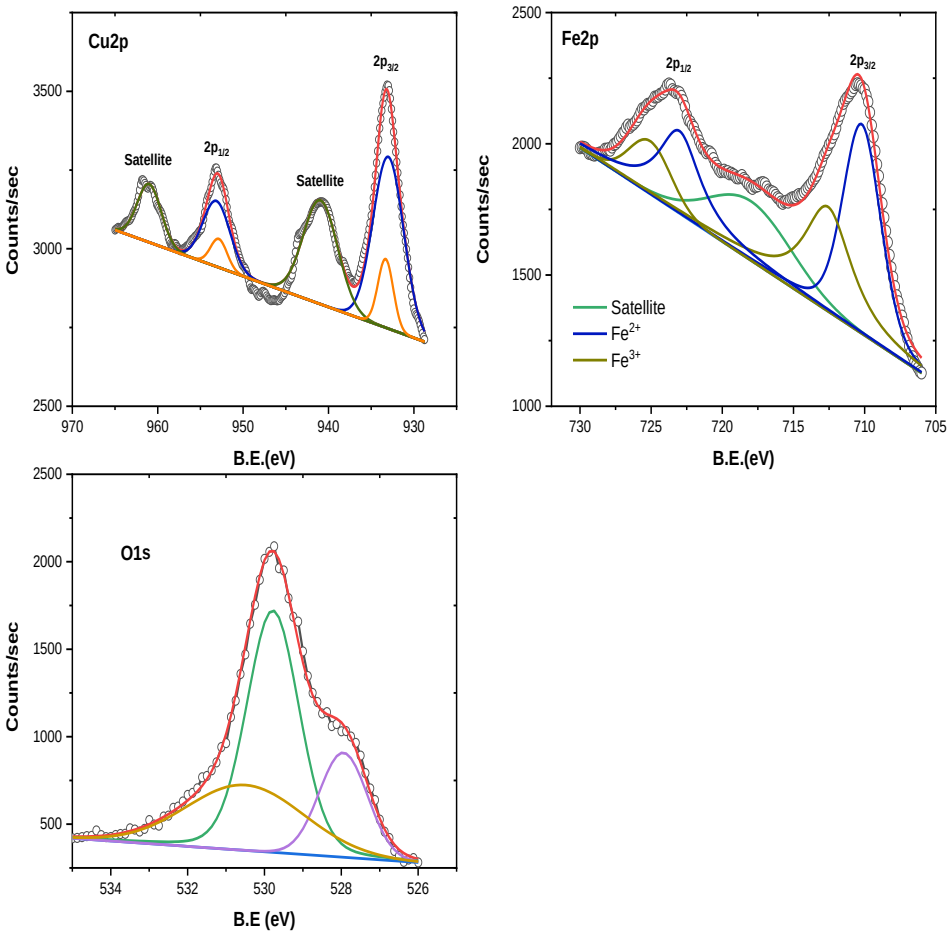

Figure 9: XPS spectra for $CuFe_2O_4$

To gain the information regarding chemical composition and the oxidation state of element, X-Ray Photoelectron Spectroscopy (XPS) were performed on $CuCe_xFe_{2-x}O_4$ (For x = 0.0 and 1.0). Figure.9 shows XPS spectra for $CuFe_2O_4$, XPS survey scan illustrate the characteristic peaks for O 1s (530.8 ev), Fe 2p (710 eV) and Cu 2p (935 eV) (Fig.9.a). High resolution narrow scan for Fe 2p in $CuFe_2O_4$ reveals Fe $2p_{3/2}$ and Fe $2p_{1/2}$ binding energy peaks at 710.0 and 723 eV, respectively (Fig.9.d). The observed binding energy values are characteristic of Fe in its +3 oxidation state. Likewise, the high-resolution narrow scan for Cu 2p in $CuFe_2O_4$ displays energy peaks of $2p_{2/3}$ and $2p_{1/2}$ at 933.14 and 953.15 eV respectively (Fig.9.c), clearly indicating that copper is in its +2 oxidation state. Further, the $CuFe_2O_4$ show a single peak for oxygen O1 s at binding energy 529.8 eV, belongs to the oxygen -2 oxidation states.

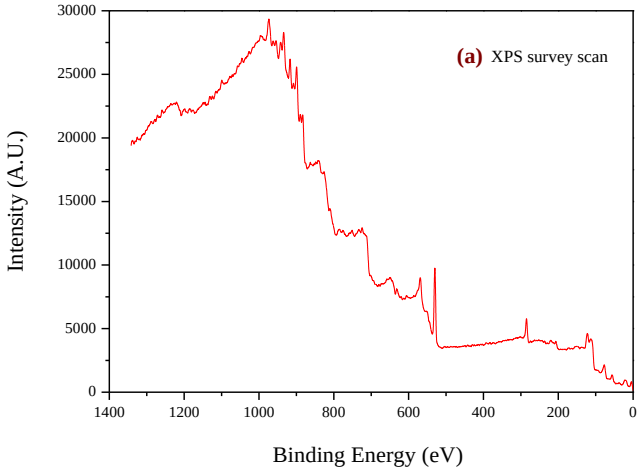
(a) XPS survey scan
Intensity (A.U.)
Binding Energy (eV)
30000
25000
20000
15000
10000
5000
0
1400
1200
1000
800
600
400
200
0

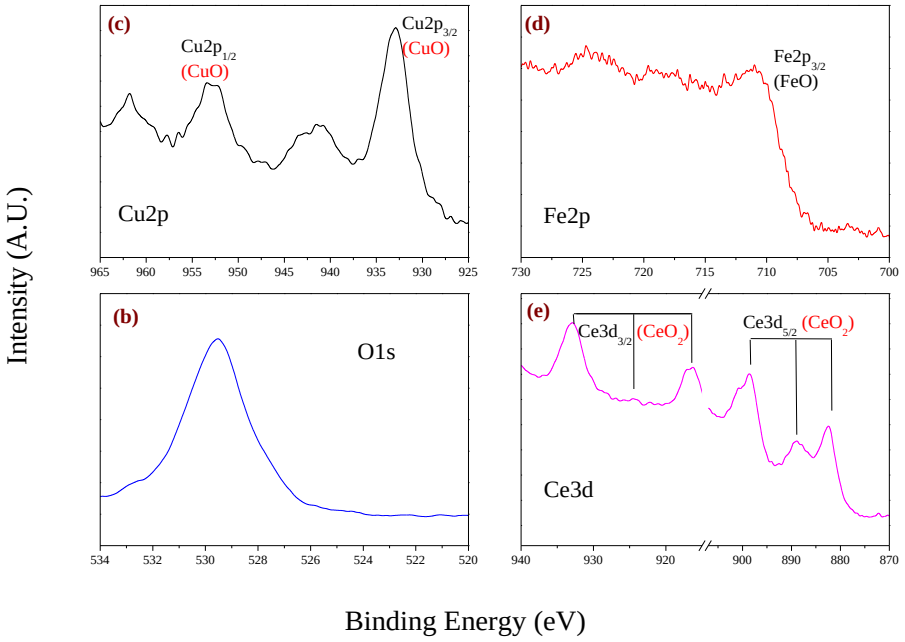
(c)
Cu2p1/2 (CuO)
Cu2p3/2 (CuO)
Cu2p
(d)
Fe2p3/2 (FeO)
Fe2p
(b)
O1s
(e)
Ce3d3/2 (CeO2)
Ce3d5/2 (CeO2)
Ce3d
Intensity (A.U.)
Binding Energy (eV)

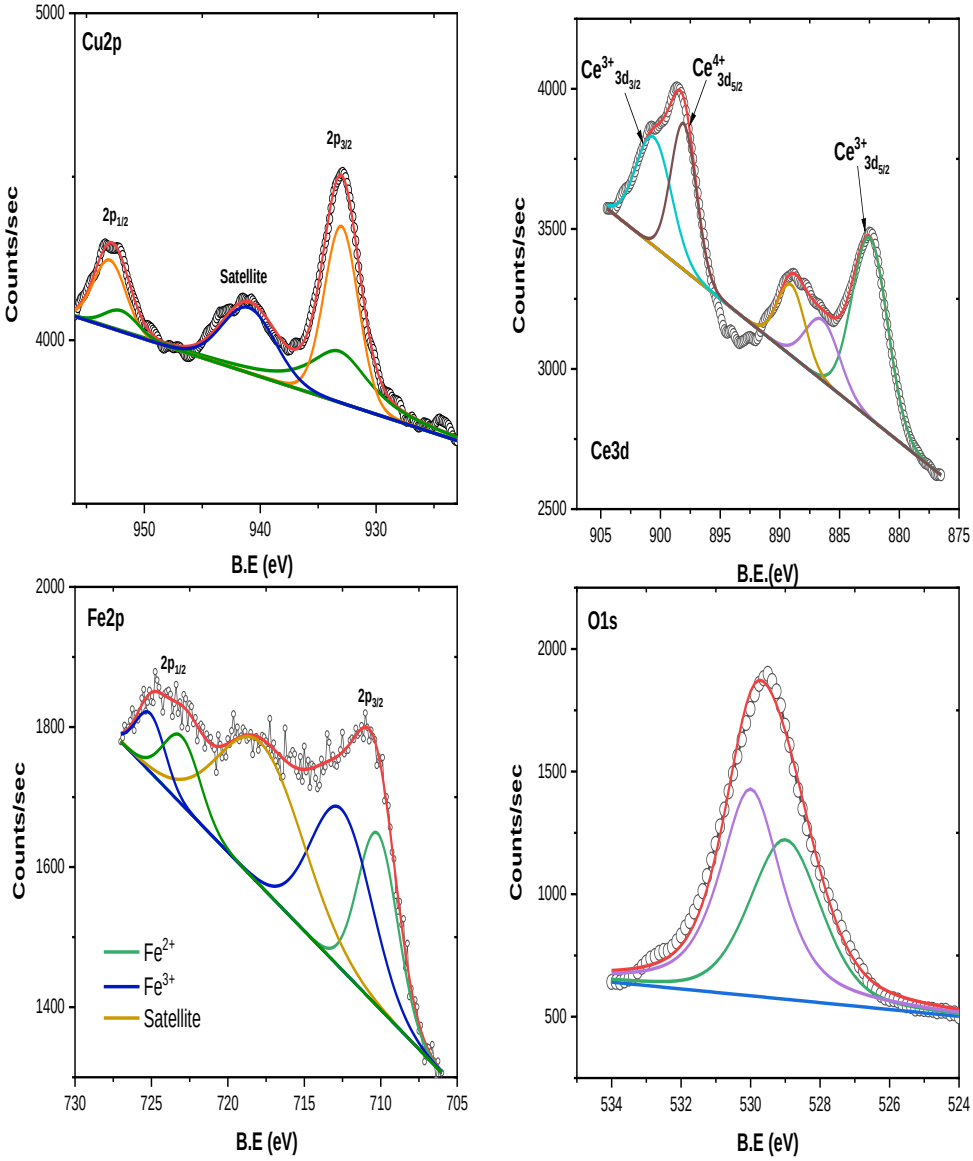

Figure 10: XPS spectra for $CuCeFeO_4$

Figure.10 shows XPS spectra for Ce^{3+} doped $CuFe_2O_4$. XPS survey scan illustrate the characteristic peaks for O 1s (530.8 ev), Fe 2p (710 eV), Ce 3d (882.53) and Cu 2p (935 eV) (Fig.10.a). High resolution narrow scan for oxygen in $CuFe_2O_4$ reveals O1 s at binding energy 529.8 eV (Fig.10.b), belongs to the oxygen -2 oxidation states. Likewise, the high-resolution narrow scan for Cu 2p in $CuFe_2O_4$ displays energy peaks of $2p_{2/3}$ and $2p_{1/2}$ at 933.14 and 953.15 eV respectively (Fig.10.c), clearly indicating that copper is in its +2 oxidation state. Further,

the $CuFe_2O_4$ show a peak for Fe $2p_{3/2}$ at binding energy 710.0 eV (Fig.10.d). The observed binding energy values are characteristic of Fe in its +2 oxidation state.

Lastly high-resolution narrow scan for Ce 3d in $CuFe_2O_4$ displays energy peaks of $3d_{5/2}$ and $3d_{3/2}$ at 882.33, 889 and 898.62 eV and 916, 924.27 and 933 eV respectively (Fig.10.e), confirming that cerium is in its +4 oxidation state. The XPS analysis is in confirmation with XRD analysis

3.7 Magnetic Measurements

The knowledge of saturation magnetization (Ms) of $CuCe_xFe_{2-x}O_4$ (with x = 0.0 to 1.0) measured at room temperature measured from hysteresis loop was as shown in Fig.11.

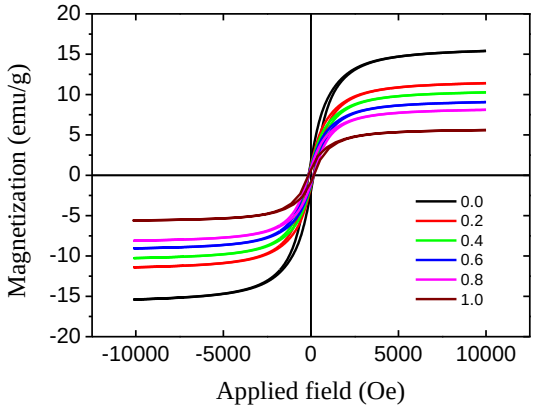

Figure 11: Variation of saturation magnetization (Ms) with applied filed for Ce^{3+} doped copper ferrite

The analysis of magnetization data, as illustrated in Figure 12, demonstrates a discernible decline in magnetic properties with the substitution of Ce^{3+} ions in $CuFe_2O_4$ nanoparticles. This reduction in saturation magnetization can be primarily attributed to the inherent magnetic moment of the doped Ce^{3+} ions, which is quantified at 2.54 µB. This value is notably lower than that of Fe^{3+} ions, which possess a magnetic moment of 5.9 µB. The observed decrease in magnetization with escalating Ce^{3+} content further compounds this effect, a phenomenon that can be explained by the progressive transformation of Fe^{3+} ions located at octahedral sites into Fe^{2+} ions at tetrahedral sites within the ferrite structure.

This ionic conversion is significant because the magnetic moment associated with Fe^{3+} ions surpass that of Fe^{2+} ions. Therefore, as the proportion of Ce^{3+} substitution increases, leading to a greater conversion of Fe^{3+} to Fe^{2+} ions, there is a consequent decline in the overall magnetization of the ferrite material. This outcome underscores the intricate relationship between ionic substitution and magnetic properties in ferrite nanoparticles, highlighting the delicate balance between enhancing certain material characteristics through doping and the potential trade-offs in magnetic performance. The detailed examination of these dynamics provides a comprehensive understanding of the effects of Ce^{3+} doping on the magnetic

behavior of $CuFe_2O_4$, offering insights into the material's suitability and potential optimizations for various technological applications where magnetic properties are paramount. [(Shirsath et al., 2011), (Rai et al., 2013)]. Also Ce ion replaces the Fe^{3+} ions at octahedral B-site which results decrease in magnetization due to the presence of CeO_2 secondary phase [(Paunović et al., 2012), (Li et al., 2010)] which is confirmed from XRD and XPS analysis. The Bohr magneton (nB) was calculated using the relation [(Smit, 1971)]

$$n_B = \frac{\text{Molecular Weight} \times \text{Ms}}{5585}$$

The magneton number decreases with Ce ions substitution increases. The variation of nB with Ce concentration was shown in Fig.12.

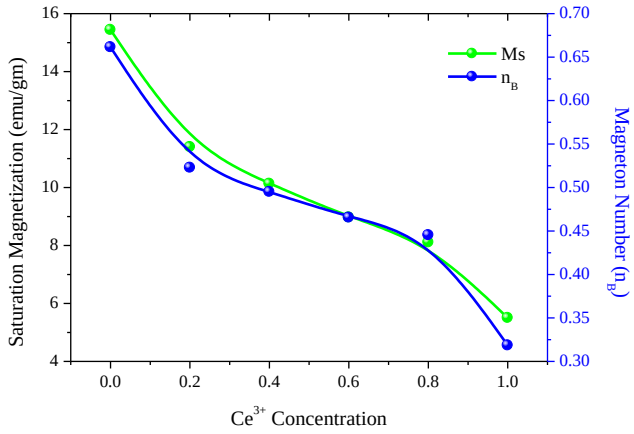

Figure 12: Variation of saturation magnetization (Ms) and magneton number (n_B) for Ce^{3+} doped copper ferrite

4. Conclusions

This study conclusively demonstrates the significant impact of cerium (Ce^{3+}) doping on the structural, morphological, and magnetic properties of $CuFe_2O_4$ nanoparticles. The synthesis of nano-crystalline Ce-doped copper ferrites through the Sol-gel auto-combustion method and their subsequent characterization via techniques such as XRD, FTIR, FESEM, TEM, EDS, and XPS have elucidated the transition from a single tetragonal ferrite phase to mixed phases with increasing Ce^{3+} concentration. This phase transition is attributed to the substitution of Fe^{3+} ions by Ce^{3+} ions at the octahedral sites, as evidenced by changes in the FTIR absorption bands and XRD patterns. The observed decrease in magnetization is linked to the formation of a CeO_2 secondary phase and the aforementioned ionic substitution. The consistency between the calculated particle sizes from SEM images and XRD analysis, along with the compositional verification through EDS, underscores the precision of the synthesis and characterization processes. This research underscores the potential of cerium doping in tailoring the properties of ferrite nanoparticles for enhanced functionality in technological

applications, despite the noted reduction in magnetization which may limit certain uses but could be advantageous in others, depending on the specific requirements of the application.

References

1. Abdellatif, M. H., Innocenti, C., Liakos, I., Scarpellini, A., Marras, S., & Salerno, M. (2017). Effect of Jahn-Teller distortion on the short range magnetic order in copper ferrite. Journal of Magnetism and Magnetic Materials, 424, 402–409. https://doi.org/10.1016/j.jmmm.2016.10.110
2. Akhtar, P., Akhtar, M. N., Baqir, M. A., Ahmad, A., Khallidoon, M. U., Farhan, M., & Khan, M. A. (2021). Structural and magnetic evaluations of rare-earths (Tb, Pr, Ce, Gd, Y)-doped spinel ferrites for high frequency and switching applications. Journal of Materials Science: Materials in Electronics, 32(6), 7692–7703. https://doi.org/10.1007/s10854-021-05487-4
3. Amiri, M., Salavati-Niasari, M., & Akbari, A. (2019). Magnetic nanocarriers: Evolution of spinel ferrites for medical applications. Advances in Colloid and Interface Science, 265, 29–44. https://doi.org/10.1016/j.cis.2019.01.003
4. Andersen, H. L., Saura-Múzquiz, M., Granados-Miralles, C., Canévet, E., Lock, N., & Christensen, M. (2018). Crystalline and magnetic structure-property relationship in spinel ferrite nanoparticles. Nanoscale, 10(31), 14902–14914. https://doi.org/10.1039/c8nr01534a
5. Bhalla, N., Taneja, S., Thakur, P., Sharma, P. K., Mariotti, D., Maddi, C., Ivanova, O., Petrov, D., Sukhachev, A., Edelman, I. S., & Thakur, A. (2021). Doping Independent Work Function and Stable Band Gap of Spinel Ferrites with Tunable Plasmonic and Magnetic Properties. Nano Letters, 21(22), 9780–9788. https://doi.org/10.1021/acs.nanolett.1c03767
6. Bhosale, J. L., Kulkarni, S. N., Sasmile, R. B., & Chougule, B. K. (1996). Susceptibility and magnetization studies of Gd3+ substituted Mg-Cd ferrites. Bulletin of Materials Science, 19(5), 767–774. https://doi.org/10.1007/BF02745197
7. Bhowmik, R. N., & Ranganathan, R. (2001). Magnetic properties in rare-earth substituted spinel Co0.2Zn0.8Fe2-xRExO4 (RE=Dy, Ho and Er, x=0.05). Journal of Alloys and Compounds, 326(1–2), 128–131. https://doi.org/10.1016/S0925-8388(01)01248-8
8. Borah, R., & Ravi, S. (2021). Effect of cation distributions on structural and magnetic properties of Ni1-xCoxFe2O4 spinel ferrites. Journal of Magnetism and Magnetic Materials, 538(July), 168276. https://doi.org/10.1016/j.jmmm.2021.168276
9. Cullity, .B. D. (1978). Elements of X-ray diffraction (3rd ed.). Addison-Wesley publishers, USA,.
10. Gadkari, A. B., Shinde, T. J., & Vasambekar, P. N. (2009). Structural analysis of Y3+-doped Mg-Cd ferrites prepared by oxalate co-precipitation method. Materials Chemistry and Physics, 114(2–3), 505–510. https://doi.org/10.1016/j.matchemphys.2008.11.011
11. Gadkari, A. B., Shinde, T. J., & Vasambekar, P. N. (2010). Magnetic properties of rare earth ion (Sm3+) added nanocrystalline Mg-Cd ferrites, prepared by oxalate co-precipitation method. Journal of Magnetism and Magnetic Materials, 322(24), 3823–3827. https://doi.org/10.1016/j.jmmm.2010.06.021
12. Jandl, S., & Deslandes, J. (1981). Infrared spectra of HfS3. Physical Review B, 24(2), 1040–1044. https://doi.org/10.1103/PhysRevB.24.1040
13. Kefeni, K. K., Mamba, B. B., & Msagati, T. A. M. (2017). Application of spinel ferrite nanoparticles in water and wastewater treatment: A review. Separation and Purification Technology, 188, 399–422. https://doi.org/10.1016/j.seppur.2017.07.015
14. Kupferling, M., Grossinger, R., Wiesinger, G., Pieper, M., & Reissner, M. (2005). Magnetic and structural properties of La-substituted ferrites. IEEE transactions on magnetics, 41(10), 3889-3891.
15. Latiff, H., Kishimoto, M., Inoue, J. ichiro, Kita, E., Yanagihara, H., & Devillers, T. (2019).

Strain-induced magnetic anisotropy via the Jahn-Teller effect and the magnetoelastic coupling of tetragonally distorted (Cu,Co)Fe2O4 particles. Journal of Magnetism and Magnetic Materials, 489(November 2018). https://doi.org/10.1016/j.jmmm.2019.165380

16. Li, M., Zhang, R., Zhang, H., Feng, W., & Liu, X. (2010). Synthesis, structural and magnetic properties of CeO2 nanoparticles. Micro and Nano Letters, 5(2), 95–99. https://doi.org/10.1049/mnl.2009.0092
17. Mahmoud, M. H., & Sattar, A. A. (2004). Mössbauer study of Cu-Zn ferrite substituted with rare earth ions. Journal of Magnetism and Magnetic Materials, 277(1–2), 101–105. https://doi.org/10.1016/j.jmmm.2003.10.016
18. Meng, X., Li, H., Chen, J., Mei, L., Wang, K., & Li, X. (2009). Mössbauer study of cobalt ferrite nanocrystals substituted with rare-earth Y3+ ions. Journal of Magnetism and Magnetic Materials, 321(9), 1155–1158. https://doi.org/10.1016/j.jmmm.2008.10.041
19. Panda, R. N., Shih, J. C., & Chin, T. S. (2003). Magnetic properties of nano-crystalline Gd- or Pr-substituted CoFe2O4 synthesized by the citrate precursor technique. Journal of Magnetism and Magnetic Materials, 257(1), 79–86. https://doi.org/10.1016/S0304-8853(02)01036-3
20. Panneer Muthuselvam, I., & Bhowmik, R. N. (2010). Mechanical alloyed Ho3+ doping in CoFe2O4 spinel ferrite and understanding of magnetic nanodomains. Journal of Magnetism and Magnetic Materials, 322(7), 767–776. https://doi.org/10.1016/j.jmmm.2009.10.057
21. Paunović, N., Dohcevic-Mitrovic, Z., Scurtu, R., Aškrabić, S., Prekajski, M., Matović, B., & Popović, Z. V. (2012). Suppression of inherent ferromagnetism in Pr-doped CeO2 nanocrystals. Nanoscale, 4(17), 5469–5476. https://doi.org/10.1039/c2nr30799e
22. Rahimi-Nasrabadi, M., Behpour, M., Sobhani-Nasab, A., & Jeddy, M. R. (2016). Nanocrystalline Ce-doped copper ferrite: synthesis, characterization, and its photocatalyst application. Journal of Materials Science: Materials in Electronics, 27(11), 11691–11697. https://doi.org/10.1007/s10854-016-5305-8
23. Rai, B. K., Mishra, S. R., Nguyen, V. V., & Liu, J. P. (2013). Synthesis and characterization of high coercivity rare-earth ion doped Sr0.9RE0.1Fe10Al2O19 (RE: Y, La, Ce, Pr, Nd, Sm, and Gd). Journal of Alloys and Compounds, 550, 198–203. https://doi.org/10.1016/j.jallcom.2012.09.021
24. Sagu, J. S., Wijayantha, K. G. U., & Tahir, A. A. (2017). The Pseudocapacitive Nature of CoFe2O4 Thin Films. Electrochimica Acta, 246, 870–878. https://doi.org/10.1016/j.electacta.2017.06.110
25. Shinde, T. J., Gadkari, A. B., & Vasambekar, P. N. (2012). Influence of Nd 3+ substitution on structural, electrical and magnetic properties of nanocrystalline nickel ferrites. Journal of Alloys and Compounds, 513, 80–85. https://doi.org/10.1016/j.jallcom.2011.10.001
26. Shirsath, S. E., Jadhav, S. S., Toksha, B. G., Patange, S. M., & Jadhav, K. M. (2011). Influence of Ce4 ions on the structural and magnetic properties of NiFe2O4. Journal of Applied Physics, 110(1). https://doi.org/10.1063/1.3603004
27. Smit, J. (1971). Magnetic Properties of Materials (Intra-Univ).
28. Subbiah, K., Han-Seung, L., Yun Su, L., Jitendra Kumar, S., Seung-Jun, K., & Rethinam, N. (2017). Fabrication of a cerium-doped nickel ferrite solid-state reference electrode and its performance evaluation in concrete environment. Sensors and Actuators, B: Chemical, 251, 509–523. https://doi.org/10.1016/j.snb.2017.05.002
29. Tahir Farid, H. M., Ahmad, I., Ali, I., Mahmood, A., & Ramay, S. M. (2018). Structural and dielectric properties of copper-based spinel ferrites. European Physical Journal Plus, 133(2). https://doi.org/10.1140/epjp/i2018-11832-4
30. Yang, Y., Jiang, J., Li, L., & Xie, Y. (2007). Synthesis and magnetic properties of nano-sized $Zn_{0.6}Cu_{0.4}Cr_{0.5}Sm_xFe_{1.5-x}O_4$ via soft chemistry route. Journal of Rare Earths, 25(Suppl. 2), 228–231. https://doi.org/10.1016/S1002-0721(07)60476-1